Interpretation of Domain Patterns Recently Found in BiMn and SiFe Alloys*

JOHN B. GOODENOUGH
Lincoln Laboratory, Massachusetts Institute of Technology, Lexington, Massachusetts
(Received January 10, 1956)

It is shown that in a demagnetized crystal in which closure domains do not form, the domain pattern on a surface perpendicular to the easy-magnetization axis varies with the thickness of the crystal. For thin crystals the domain configuration should consist of plane-parallel walls. As the thickness of the crystal is increased, the plane walls become undular to form a rickrack-type pattern, the amplitude of the waves increasing with increasing thickness. At greater thicknesses the domain pattern becomes more complicated, a characteristic feature being many small domains of reverse magnetization penetrating as spikes from the surface into the interior. A typical pattern for a demagnetized sample could consist of a regular pattern of reverse-domain spikes within large domains demarked by plane-parallel walls extending all the way through the crystal. These theoretical predictions are compared with domain patterns recently observed in BiMn alloys and in barium ferrite. Recently reported domain patterns in polycrystalline SiFe alloys are interpreted as representing the latter thick-crystal configuration. The significance of the patterns found in SiFe alloys for the theory of flux reversal is also discussed.

I. INTRODUCTION

ROBERTS and Bean[1] have used plane-polarized light in reflection to observe magnetic-domain patterns in ferromagnetic BiMn alloy. This alloy has the hexagonal (NiAs) crystal structure, a single axis of easy magnetization along the c-axis, and a large anisotropy constant[2] ($K \approx 10^7$ ergs/cm^3). The anisotropy is sufficiently large to inhibit closure-domain formation; there exist in the crystal only 180° domain walls which are nearly parallel to the c-axis. Consequently there is a large surface density of free magnetic poles on any surface of the crystal making a large angle with the c-axis. The energy associated with these magnetic poles and with the 180° domain walls will alone determine the domain patterns observed on the surface.

Roberts[1] observed that the domain patterns on polished surfaces perpendicular to the c-axis depended upon the thickness of the crystal. In thin crystals the patterns consisted essentially of plane-parallel walls. In thicker crystals the patterns became undular, the amplitude of the rickrack waves increasing with crystal thickness. In the thickest crystals they found considerably more complicated patterns such as those reported earlier by Williams, Foster, and Wood[3] on (0001) surfaces of hexagonal cobalt. After an external field had been applied perpendicular to a surface on which rickrack patterns were observed, the remanent rickrack patterns were broken up into separate domain regions, some of which were rings with six sides. This led Roberts and Bean to suggest that perhaps the six-sided rings reflect the hexagonal symmetry of the lattice.

In Sec. II there is a qualitative discussion, in Sec. III a quantitative calculation, of the energy associated with the surface magnetic poles in a ferromagnetic material with various magnetic-domain configurations. There is also a discussion of the character of the domains to be expected within the bulk of the material as the thickness of the crystal varies. From this discussion it is shown that the rickrack and six-sided ring patterns can be understood from a consideration of the energies associated with the surface poles and the domain walls; it is not necessary to assume that they are associated with the hexagonal symmetry of BiMn alloy.

In Sec. IV there is a discussion of the domain patterns recently observed by Paxton and Nilan[4] in thin ribbons of SiFe alloy. The patterns of interest were observed in grains in which there was no closure-domain formation. Although Paxton and Nilan suggested that their observations were incompatible with a theory of reverse-domain nucleation at grain boundaries[5] and the consequent flux-reversal mechanism in metallic-tape cores,[6] it is shown that the observed domain patterns can be readily interpreted in terms of the physical concepts on which the grain-boundary nucleation and flux-reversal mechanisms were based.

II. QUALITATIVE DISCUSSION

It has previously been pointed out by various workers[7] how the energy associated with the demagnetizing fields in a ferromagnetic sample magnetized perpendicular to two parallel surfaces of the material may be greatly reduced by the creation of parallel 180° domain walls; such a wall configuration causes parallel strips of alternately south and north poles to appear on the surfaces. If closure domains do not form, the optimum separation for these walls can be readily calculated by balancing the surface-pole energy gain due

* The research in this document was supported jointly by the Army, Navy, and Air Force under contract with the Massachusetts Institute of Technology.

[1] B. W. Roberts and C. P. Bean, Phys. Rev. **96**, 1494 (1954); B. W. Roberts, Conference on Magnetism and Magnetic Materials, Pittsburgh, Pennsylvania (June 14–16, 1955), Am. Inst. Elec. Eng. (October, 1955), p. 192.

[2] C. Guillaud, J. phys. radium **12**, 492 (1951).

[3] Williams, Foster, and Wood, Phys. Rev. **82**, 119 (1951).

[4] W. S. Paxton and T. G. Nilan, J. Appl. Phys. **26**, 994 (1955).

[5] J. B. Goodenough, Phys. Rev. **95**, 917 (1954).

[6] N. Menyuk and J. B. Goodenough, J. Appl. Phys. **26**, 8 (1955).

[7] See the review article by C. Kittel, Revs. Modern Phys. **21**, 541 (1949).

to reducing the separation of these walls with the domain-wall energy loss due to increasing the total area of domain wall present. However, there are other possible domain-wall configurations which, in the absence of closure-domain formation, may give even lower total-energy states.

The reduction in surface-pole energy by the creation of alternate rows of north and south poles is due to the formation of smaller flux-closure paths for the demagnetizing fields associated with the free magnetic poles. This reduction in surface-pole energy would be even greater if the flux-closure paths were reduced in all directions of the planar surface instead of in just one. Since any reduction in flux-closure path length can only occur at the expense of more domain-wall area, the problem is to imagine that configuration which gives an optimum balance between the two energies.

There are two possible configurations for the demagnetized state which would give small surface-pole energies, the checkerboard array of Fig. 1(a) and the circular array of Fig. 1(b). The wall area associated with Fig. 1(a) is considerably reduced without an appreciable increase in the surface-pole energy if the corners are rounded as in Fig. 1(c) (see Sec. III); but this is immediately seen to closely approximate the rickrack pattern observed by Roberts and Bean.[1]

The configurations of Fig. 1(d) are seen to be a combination of the rickrack and circular patterns; such configurations were found by Roberts and Bean on some areas of a (0001) surface of BiMn alloy after it had been subject to a perpendicular magnetic field of 15 000 oersteds.

The problem, then, is to calculate quantitatively the optimum rickrack configuration and compare its energy with the configuration of plane parallel walls. If the optimum rickrack configuration is roughly that observed by Roberts and Bean and is of lower total energy than a plane-wall configuration, the rickrack patterns do not illustrate any new principle.

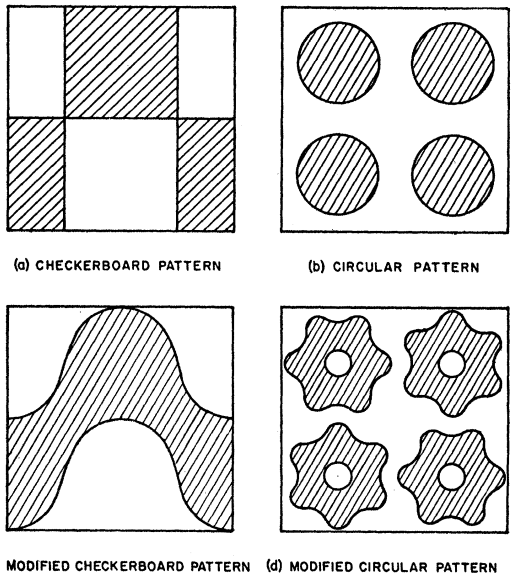

FIG. 1. Domain configurations with low demagnetizing-field energy.

III. MATHEMATICAL DEVELOPMENT

The principal mathematical problem is to develop an expression for the energy associated with an arbitrary distribution of magnetic poles on a plane surface of magnetic material. The treatment to be used here is essentially that outlined by Kittel.[7]

It is assumed that the surface magnetic-pole density $\omega^*=\omega^*(x,y)$ is periodic in a fundamental area of sides $2\pi L_x$ and $2\pi L_y$ so that it can be expressed by a double Fourier series as

$$\omega^*(x,y)=\sum_{-\infty}^{\infty}\sum_{-\infty}^{\infty}C_{mn}e^{i(m\xi+n\eta)},$$

where $\xi=x/L_x$, $\eta=y/L_y$ and

$$C_{mn}=\frac{1}{4\pi^2}\int_0^{2\pi}\int_0^{2\pi}\omega^*(\xi,\eta)e^{-i(m\xi+n\eta)}d\eta d\xi.$$

If the plane surface is the surface of a material with spontaneous magnetization I_s which is oriented along the z-axis perpendicular to the plane, the magnetic energy per unit area is

$$\sigma_m=-\tfrac{1}{2}\int_{-L}^{0}\mathbf{H}\cdot\mathbf{I}_s dz,$$

where L is the length of the specimen along the z-axis. The demagnetizing field H due to magnetic poles is perpendicular to the plane so that $\mathbf{H}=\mathbf{k}H_z$ and

$$H_z=-\partial\phi/\partial z,\quad \nabla^2\phi=0.$$

Since $\mathbf{B}=\mathbf{H}+4\pi\mathbf{I}_s$ must be continuous across the plane, there is the boundary condition

$$H_z^0=-\left.\frac{\partial\phi}{\partial z}\right|_{z=0}=\mp 2\pi\omega^*(x,y).$$

In order to obtain a function which satisfies this boundary condition, let

$$\phi_{mn}=-\frac{1}{P_{mn}}(H_z^0)_{mn}e^{P_{mn}z}.$$

Substitution of ϕ_{mn} into the Laplacian gives

$$P_{mn}=\left\{\left(\frac{m}{L_x}\right)^2+\left(\frac{n}{L_y}\right)^2\right\}^{\frac{1}{2}}.$$

Therefore,

$$H_z=-\partial\phi/\partial z=\mp 2\pi\omega^*(x,y)e^{P_{mn}z},$$

and

$$\sigma_m=\pi\int_{-L}^{0}\omega^*(x,y)\bar{\omega}^*(x,y)e^{P_{mn}z}dz,$$

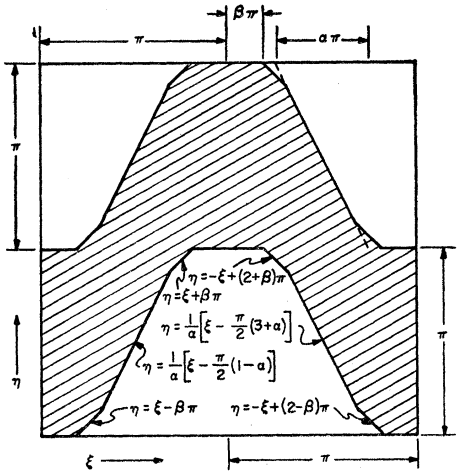

FIG. 2. Surface-pole configuration used in calculations of energy associated with rickrack domain patterns.

where I_s is taken as $\bar{\omega}^*(x,y)$ to insure that H_z and I_s always point in opposite directions. It follows that

$$\sigma_m=\pi C_{00}{}^2L+\pi\sum_{\substack{-\infty\\(\text{excluding}\\ m=n=0)}}^{\infty}\sum_{-\infty}^{\infty}C_{mn}C_{-m-n}P_{mn}{}^{-1}(1-e^{-P_{mn}L}). \quad (1)$$

In the demagnetized state the areas of north and south poles are equal so that $C_{00}=0$. Further, in most cases of interest $e^{-P_{mn}L}\ll 1$ so that

$$\sigma_m=\pi\sum_{\substack{-\infty\\(\text{excluding}\\ m=n=0)}}^{\infty}\sum_{-\infty}^{\infty}C_{mn}C_{-m-n}P_{mn}{}^{-1}. \quad (2)$$

Using Eq. (2), Kittel[7] calculated the energy per unit area of a checkerboard array corresponding to Fig. 1(a) to be

$$\sigma_m{}^{(1a)}=0.53\omega^{*2}D^{(1a)},$$

where $D^{(1a)}$ is the side of each minor square. Similarly he calculated the energy per unit area of the configuration corresponding to Fig. 1(b) to be

$$\sigma_m{}^{(1b)}=0.374\omega^{*2}D^{(1b)},$$

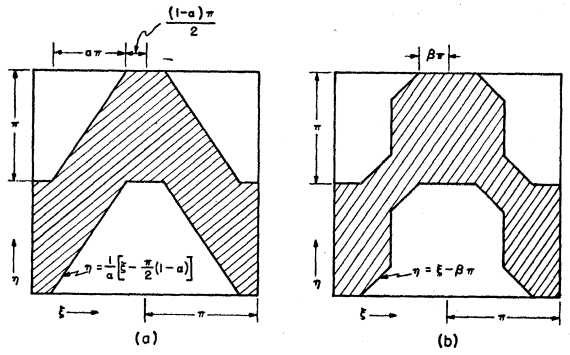

FIG. 3. Surface-pole configurations for (a) $\beta=(1-\alpha)/2$, (b) $\alpha=0$.

where the fundamental area is a square of side $D^{(1b)}$ in which there is imbedded a circle of opposite polarity of radius $D^{(1b)}/(2\pi)^{\frac{1}{2}}$. He showed that the energy per unit area associated with planar strips of alternating polarity and width D' is

$$\sigma_m=0.8525\omega^{*2}D'.$$

The total energy per unit top surface of a bar magnet of length L is therefore

$$\sigma_wL/D'+1.7\omega^{*2}D',$$

where σ_w is the domain-wall energy per unit area of wall. This total energy is a minimum with respect to the domain width D' if $\sigma_wL/\omega^{*2}D'^2=1.7$.

The change in bar-magnet energy per unit top-surface area from the parallel-strip configuration to the configuration of Fig. 1(a) or Fig. 1(b), respectively, can therefore be written as

$$\Delta\sigma^{(1a)}=\omega^{*2}D'\{3.4-1.06(D^{(1a)}/D')-3.4(D'/D^{(1a)})\},$$

$$\Delta\sigma^{(1b)}=\omega^{*2}D'\{3.4-0.75(D^{(1b)}/D')-1.7(2\pi)^{\frac{1}{2}}(D'/D^{(1b)})\}.$$

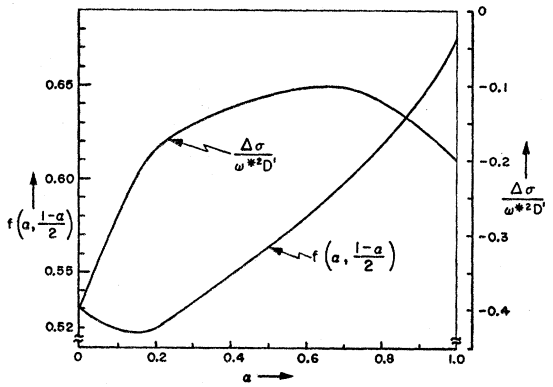

FIG. 4. $\Delta\sigma/\omega^{*2}D'$ and $f(\alpha,\beta)$ *vs* α for $\beta=(1-\alpha)/2$, $L_x=L_y$.

The optimum values for $D^{(1a)}$ and $D^{(1b)}$ are $1.8D'$ and $2.4D'$, respectively; and the corresponding energy changes are $\Delta\sigma^{(1a)}=-0.4\omega^{*2}D'$ and $\Delta\sigma^{(1b)}=-0.2\omega^{*2}D'$. It is not, therefore, immediately obvious that the configuration of parallel strips of alternate polarity can be replaced by a more stable one. It should be noted, however, that the walls are assumed to remain perpendicular to the surface. The relaxation of this condition is discussed later. It is of interest to determine first whether the energy change $\Delta\sigma$ can be positive for any configuration of surface poles if the walls remain everywhere perpendicular to the surface and pass through the crystal.

To calculate the energy associated with the modified checkerboard pattern of Fig. 1(c), the configuration of Fig. 2 is used. This configuration has an integrable solution and contains two parameters, α and β, which can be varied within the limits $0\leq\alpha\leq 1$ and $0\leq\beta\leq(1-\alpha)/2$. If $\beta=(1-\alpha)/2$, the configuration is the

trapezoidal pattern of Fig. 3(a) and varies from the checkerboard pattern for $\alpha=0, \beta=\frac{1}{2}$ to a zigzag pattern for $\alpha=1$, $\beta=0$. Similarly if $\alpha=0$, the configuration is the snipped-corner checkerboard pattern of Fig. 3(b) which varies from the checkerboard pattern for $\beta=\frac{1}{2}$ to the zigzag pattern for $\beta=0$. The details of the calculation of $f(\alpha,\beta)=\sigma_m/\omega^{*2}D$ from Eq. (2) and of the change in energy per unit top-surface area $\Delta\sigma$ are given in Appendix I.

It was first assumed that $L_x=L_y$. In Fig. 4 are plotted the calculated curves for $f(\alpha, (1-\alpha)/2)$ and $\Delta\sigma/\omega^{*2}D'$ as a function of the parameter α, and in Figs. 5 and 6(a) the calculated curves for $\Delta\sigma/\omega^{*2}D'$ and $f(0,\beta)$, $f(\frac{1}{2},\beta)$ *vs* the parameter β. For no value of α and β is $\Delta\sigma>0$. Since the optimum value for β appears to be $\beta=(1-\alpha)/4$, the calculated values of $\Delta\sigma/\omega^{*2}D'$ and $f(\alpha, (1-\alpha)/4)$ *vs* α are plotted in Fig. 6(b). From this plot it is apparent that the optimum shape, under the assumptions of Fig. 2, is a configuration with $\alpha=\frac{1}{2}$, $\beta=\frac{1}{8}$; but even this optimum configuration has $\Delta\sigma<0$ so that it is a less

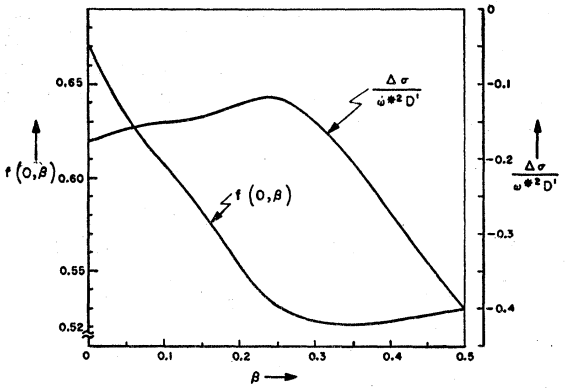

FIG. 5. $\Delta\sigma/\omega^{*2}D'$ and $f(\alpha,\beta)$ *vs* β for $\alpha=0$, $L_x=L_y$.

stable configuration than that of alternating parallel strips of positive and negative magnetic poles.

In Appendix II the restriction $L_x=L_y$ is removed and an additional parameter $\gamma=L_y/L_x$ is introduced. Since the optimum shape for $\gamma=1$ was seen to occur for $\alpha=\frac{1}{2}$, the surface-pole energy per unit area $f(\alpha,\beta,\gamma)\omega^{*2}D$ was calculated as a function of γ for the configuration $\alpha=\frac{1}{2}$, $\beta=(1-\alpha)/2=\frac{1}{4}$. From Fig. 7 where $f(\frac{1}{2},\gamma)$ *vs* γ is plotted it is seen that although the surface-pole energy decreases with increasing γ, the change in total energy per unit area from the plane-parallel configuration is negative, $\Delta\sigma<0$, for all values of γ. It is apparent that so long as the domain walls remain perpendicular to the surface of the material, the lowest energy configuration consists of a set of plane, parallel walls.

Although the assumption that the walls remain everywhere perpendicular to the surface gives the minimum domain-wall area in the case of plane, parallel walls, it does not provide for the minimum wall area when the walls are waved as in the rickrack patterns.

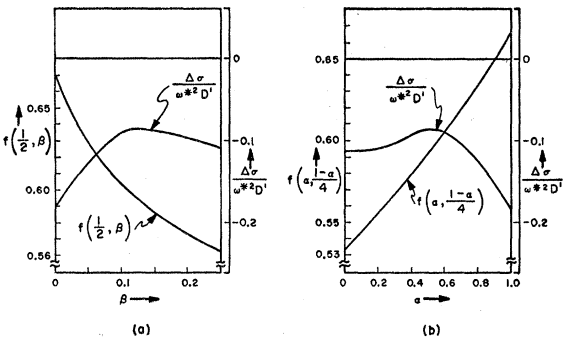

FIG. 6. $f(\alpha,\beta)$ and $\Delta\sigma/\omega^{*2}D'$ *vs* (a) β for $\alpha=\frac{1}{2}$, and (b) α for $\beta=(1-\alpha)/4$, $L_x=L_y$.

If the amplitude of the waves decreases regularly with depth of penetration into the material as illustrated in Fig. 8, there is a considerable decrease in the total wall area. In order that such a taper of amplitude exist, however, the 180° domain walls can no longer be parallel to the magnetization, and magnetic poles are associated with the domain walls. The decrease in energy due to the reduction in wall area causes the appearance of energy associated with the domain-wall poles; this energy per unit top-surface area is defined as σ_d. The appearance of this energy defines an optimum rate of change of wave amplitude with penetration depth.

In Appendix II the special case is considered in which

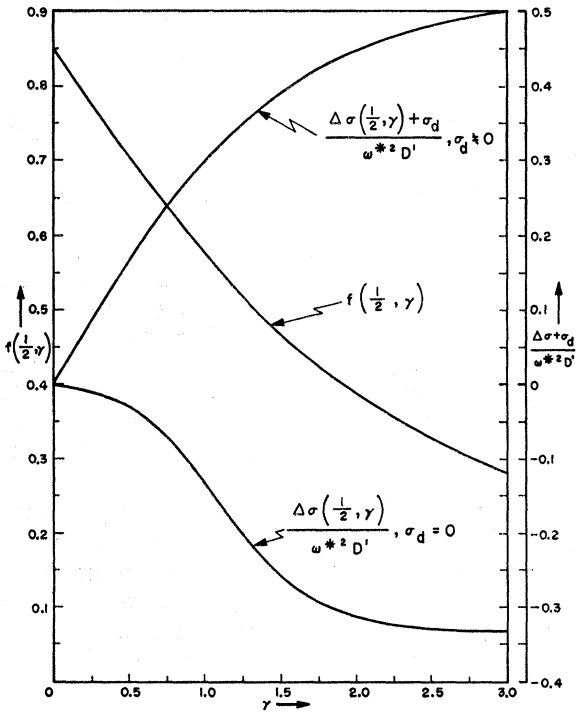

FIG. 7. $f(\frac{1}{2},\gamma)$ *vs* γ; $[\Delta\sigma(\frac{1}{2},\gamma)+\sigma_d]/\omega^{*2}D'$ *vs* γ, for walls everywhere perpendicular to the surface ($\sigma_d=0$) and for walls which taper to plane walls at the crystal half-width ($\sigma_d\neq 0$).

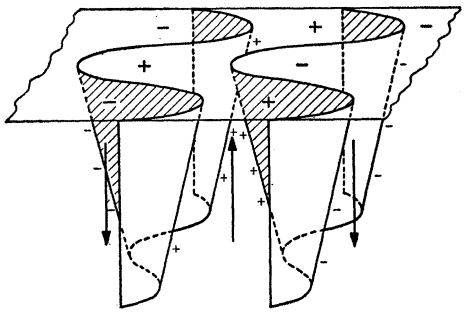

FIG. 8. Schematic domain walls with taper.

the amplitude of the waves decreases regularly to zero at the half-thickness $L/2$, then increases regularly to full amplitude at the opposite face. The energy per unit top-surface area $(\Delta\sigma+\sigma_d)$ is plotted in Fig. 7 for the domain configuration $\alpha=\frac{1}{2}, \beta=(1-\alpha)/2=\frac{1}{4}$; this energy is seen to be positive for all values of γ. Since σ_d is proportional to some positive power of D/L where $D/L=(D/D')(D'/L)\propto L^{-\frac{1}{2}}$, the term σ_d can be reduced to $\sigma_d<\sigma_d+\Delta\sigma$ by increasing the crystal thickness L. It is at once apparent that $\Delta\sigma>0$ for a crystal thickness in the neighborhood of (D/λ), where $(D/2\lambda)$ is the distance required for the surface-wave amplitude to decrease to zero at the optimum rate of wave-amplitude reduction with penetration depth.

It can be concluded that in crystals which are too thin to permit a significant change in wave amplitude within their interior, the configuration of plane, parallel walls is the most stable. For a thicker crystal wavy walls are more stable than plane walls, the amplitude of the waves increasing with thickness. However, the amplitude will not increase indefinitely: Fig. 7 indicates that the maximum amplitude probably occurs for $\gamma\lesssim 3$. Also the domain width is greater than that calculated for the plane-wall case since, by Appendix II, $D/D'>1$. This fact was observed by Roberts.[1]

Qualitatively it can be seen that for very thick crystals the configuration of Fig. 9 will form in preference to a rickrack pattern of very large amplitude. In this configuration the surface-pole energy is similar to that for a configuration of large amplitude, but the domain-wall energy is considerably reduced by the formation of rows of domains of reverse magnetization which penetrate as spikes only partially through the crystal, these rows being separated by plane-parallel walls which extend entirely through the crystal. Sixtus[8] has found patterns of this latter type on a polished surface of barium ferrite parallel to the hexagonal axis. He also reports the rickrack patterns for a surface perpendicular to the c-axis in this material.

If reverse-domain formation is more stable than a rickrack pattern, there are many complex configurations which can occur depending upon the magnetic history of the specimen. The ring patterns observed by Roberts and Bean when the BiMn specimen was subject to a large field along the c-axis are typical for a partially magnetized sample. Since the energy associated with the surface magnetic poles is large, the domains which are oriented parallel to the applied field grow as a result of a variation in the rate of taper of the rickrack walls, the cost of increased domain-wall pole energy being somewhat compensated by decreasing wall area. The changes in surface configuration will not appreciably increase the large energy associated with the surface magnetic poles until extremely large fields are applied. Consequently the surface configuration is seen to break up irreversibly into smaller units than the rickrack pattern, units such as the rings shown in Fig. 1(d), which penetrate as relatively blunt spikes into the material; the change in surface-pole energy with change in surface configuration is small.

From these considerations the interesting rickrack and ring patterns observed by Roberts and Bean are found to be due to normal energy considerations; there is no need to attribute them to the hexagonal symmetry of the lattice except insofar as this gives a unique easy axis of magnetization with large anisotropy so that closure domains do not form.

IV. PATTERNS IN SiFe ALLOY

The absence of closure domains at the surface of a magnetic material need not be associated with crystals which have but a single axis of easy magnetization and a high crystalline anisotropy, such as BiMn alloy. If the surface of a cubic crystal cuts the three axes of easy magnetization, for instance, there is no easy-magnetization direction parallel to the surface, and surface poles exist. Although closure domains may reduce the energy associated with these surface poles, it is easy to imagine a situation where this is not the case.

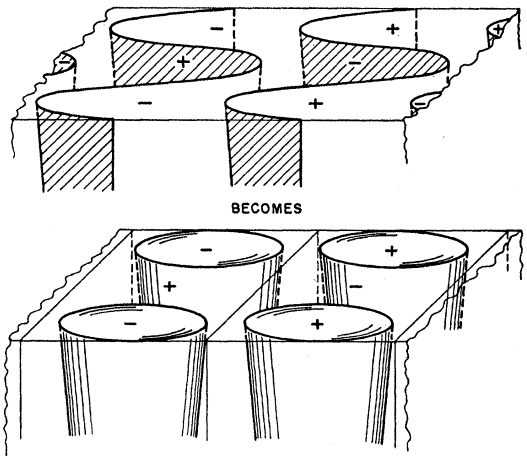

FIG. 9. Thick crystals in demagnetized state: large-amplitude rickrack pattern gives way to rows of spikes separated by plane walls.

[8] K. J. Sixtus, Conference on Magnetism and Magnetic Materials, Pittsburgh, Pennsylvania (June 14–16, 1955), Am. Inst. Elec. Eng. (October, 1955), p. 142.

Consider a strip of commercially grain-oriented 3¼% silicon steel approximately 0.01 in. thick, such as that used by Paxton and Nilan[4] in recently reported domain-pattern studies. In their work they introduced three angular parameters to define the orientation of a given grain with respect to the rolling plane and rolling direction customarily used for reference in sheet steel. The [100] direction is taken as that one of the ⟨100⟩ directions which makes the smallest angle with the rolling plane; this smallest angle is ϕ. The angle the projection of the [100] direction on the rolling surface makes with the rolling direction is θ, and α measures the degree of rotation of the [010] and [001] directions about the [100] direction, a position in which they make equal angles with the rolling plane being the reference position $\alpha=0$. Since the ⟨100⟩ directions are the easy axes of magnetization, the energy due to crystalline and demagnetization anisotropy is minimized when the magnetization is roughly parallel to the [100] direction; closure-domain formation does not reduce the energy. This particular example is chosen as the experiments reported there appear to illustrate the pattern proposed in Fig. 9. They also confirm the concepts on which an earlier theory of flux reversal was based.[5,6]

The patterns of particular interest for this discussion are those Paxton and Nilan classified as "lozenges," a pattern which was observed for $4°<\phi<7°$. The lozenge figures resemble small spikes which are either open or closed at the base and point in the [100] direction. These figures are periodically spaced in rows with a regular spacing between the rows. In the demagnetized state the lozenges are all of uniform size.

Whereas Paxton and Nilan judged that the lozenge figures are a flux-closure pattern, this conclusion can be ruled out immediately from energy considerations; closure-domain formation would only increase the magnetic-pole strength at the surface. The lozenge patterns must enclose surface regions of opposite polarity. Further, the lozenge shape is what would be anticipated for domains of reverse magnetization; proposed domains of reverse magnetization are illustrated in Fig. 10. Finally, the periodicity of the lozenges in the respective rows suggests that these reverse domains have been created to reduce the energy associated with the surface magnetic poles; the assumption of periodicity in the Fourier analysis of Sec. III is apparently quite generally valid.

The most interesting feature of the lozenge pattern, however, is its reaction to an external field applied

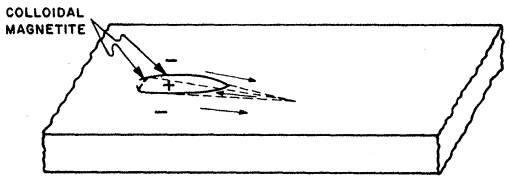

FIG. 10. Model for reverse-domain spike responsible for a lozenge.

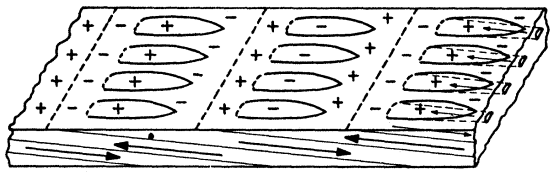

FIG. 11. Complete magnetic-domain model for lozenge patterns.

roughly parallel to the [100] direction. In such a field the lozenges of alternate rows grow, the others decrease. When the field is reversed, the set of larger lozenges decreases, of smaller lozenges increases. Such a behavior can be understood if it is postulated that invisible, parallel plane walls exist between the rows.[9] The postulated domain pattern is shown in Fig. 11; it corresponds to the thick-crystal configuration of Fig. 9. However, there are three questions which must be answered: (1) Why are only the lozenge patterns observed by colloidal-magnetite techniques? (2) Is the spacing between lozenge rows compatible with the optimum spacing D' for a configuration of plane walls parallel to the magnetization vector? (3) Why does a strip of silicon iron only 0.01 in. thick have a configuration corresponding to the predictions for a thick crystal?

The answer to the first question is readily apparent. The colloidal magnetite is attracted to the region of the surface intercepted by a wall if the atomic moments within the wall make large angles with the surface. Since the atomic moments within a 180° wall are always within the plane of the wall, only that portion of domain wall intersecting the surface at a large angle will contain atomic moments which are so directed that they attract the colloidal magnetite more strongly than the surface atomic moments within the domains themselves. The plane walls of Fig. 11 intersect the surface at a small angle; $\phi<7°$. The atomic moments within these walls make even smaller angles with the surface than do those within the domains; there can be no attraction of colloidal magnetite to the intersection of the wall with the surface. Similarly the base of each lozenge pattern consists of a wall making a small angle with the surface: this accounts for the fact that many of the lozenge figures have open bases. The fact that some are closed can be the result of fringe fields from the side walls of the lozenges which make large angles with the surface (see Fig. 10). These closures do not necessarily reflect the configuration of the base wall.

To calculate the optimum spacing for a configuration of plane-parallel walls of the type shown in Fig. 11, let the angle the walls and the magnetic moments within the domains make with the surface be $\phi'<\phi$. The demagnetizing fields rotate the magnetic moments out of the easy-magnetization direction [100] to make $\phi'<\phi$ where $\phi-\phi'=H_dI_s/2K$, H_d, I_s, and K being

[9] The possibility that invisible parallel walls exist was suggested to us by W. S. Paxton and T. G. Nilan during an informal discussion of their work.

respectively the demagnetizing field, the saturation moment, and the crystalline anisotropy constant.[7] Then the total energy per unit top surface area of a system of plane-parallel walls like that of Fig. 11 (omitting the lozenges) is

$$\sigma=\sigma_w h/(D'\sin\phi')+f_m\omega^{*2}D',$$

where $\sigma_m=f_m\omega^{*2}D'$ is the magnetic energy per unit area associated with the parallel strips of magnetic poles of surface magnetic-pole density $\omega^*=I_s\sin\phi'$. If the tape thickness h were large and ϕ' were 90°, then $f_m=0.8525$. In order to take advantage of this knowledge, assume hypothetical surfaces perpendicular to the plane walls and separated by a distance $L=h/\sin\phi'$. For these surfaces $\omega^*=I_s$ and $f_m=0.8525$ so that as in Sec. III the optimum value for wall separation is $(\sigma_w L/1.7I_s^2)^{\frac{1}{3}}$. From this it follows that for $3\frac{1}{4}\%$ silicon iron with $h=0.01$ in., $\sigma_w\approx 1$ erg/cm², $\phi'=4°$, $B_s=19.7\times10^3$ gauss,

$$D'=\frac{1}{I_s\sin\phi'}\left(\frac{\sigma_w h}{1.7\sin\phi'}\right)^{\frac{1}{3}}\approx 10^{-3}\text{ cm}.$$

Since the observed spacing between rows of lozenges in the demagnetized sample was about 10^{-2} cm, the proposed invisible walls are energetically feasible. The wider observed spacing is easily accounted for by the existence of the reverse-domain spikes in addition to the plane walls. If the observed spacing had been smaller, however, the invisible walls would not have been energetically feasible.

The answer to the third question is simply that it is not the crystal thickness, but the effective crystal thickness $L=h/\sin\phi'\approx 3.6$ mm which determines the surface domain configuration. If the ratio of minor to major dimension of the reverse-domain spike is about 1/30, the length of the reverse domains represented by the lozenges is about 0.5 mm, or $L/7$. The rickrack pattern is most stable if this length is about $L/2$; the effective thickness $L=h/\sin\phi'$ does correspond, therefore, to the thick-crystal case so that a domain configuration corresponding to Fig. 9, or Fig. 11, is to be expected.

Once the configuration of Fig. 11 is accepted, the interesting behavior of the lozenge patterns becomes obvious. The invisible parallel walls of the configuration are the mobile walls in the presence of soft magnetic fields. In the presence of an external field roughly parallel to the [100] direction, those large domains which are oriented parallel to the field grow, those oriented antiparallel shrink because of the motion of the invisible parallel walls. Since the lozenge patterns are due to reverse domains which are enclosed within these larger domains, these grow or shrink with the host domain. It should be noted that these reverse domains grow or shrink against the forces from the externally applied field; the energy associated with the surface magnetic poles is apparently larger than that associated with the external field.

Finally, these experimental results give interesting confirmation to the concepts set forth in an earlier paper.[5] First, the magnitude of the domains of reverse magnetization varies in a regular way with the size of the parent domain within which it is created. This was the basic assumption required for the term in the coercive force which varies inversely with the mean grain diameter.

Second, the domains of reverse magnetization are created in a periodic manner, an assumption which was used for the calculation of the energy associated with planes of magnetic poles. There is a correction to be made in Sec. III part B of that paper, however. If cylindrical domains of reverse magnetization are created at a planar surface with base radius r in elementary, periodic areas D^2, the energy associated with the surface magnetic poles is, according to Eq. (1),

$$\sigma_m=\pi C_{00}^2 L+(\text{harmonic terms})$$
$$=\sigma_0[(2\pi r^2/D^2)-1]^2+(\text{harmonic terms}),$$

where $\sigma_0=\pi\omega^{*2}L/3$ if the planar surface is the boundary of a grain of diameter L. The factor $\frac{1}{3}$ appears after account is taken of the finite dimensions of a grain-boundary surface. In the earlier paper the expression was given as

$$\sigma_m=\sigma_0|(2\pi r^2/D^2)-1|+(\text{harmonic terms}).$$

It follows, therefore, that the field required to move the wall irreversibly against the surface magnetic poles is

$$H_w(\omega^*)\approx\frac{\pi\omega^{*2}}{6I_s}\times 2\left(\frac{2\pi r^2}{D^2}-1\right),$$

which reduces to the value given previously for the contribution to the coercive force due to grain-boundary magnetic poles when $r\approx D/2$. Since $r=D/2$ is the value of r at which periodically distributed reverse domains meet one another, $\pi\langle\omega^{*2}\rangle/(6I_s)$ remains the only reasonable value to take for this contribution to the coercivity and all the conclusions of the earlier paper remain valid.

In the third place it was assumed that in soft magnetic materials the domains of reverse magnetization which grow to reverse the flux in the core are created within the bulk of the material, the poles at the surface of the material being so large that the reverse domains at the surface are restricted to small changes only. The lozenge patterns indicate this to be the case, the reverse domains growing against the applied field for values of ϕ as low as 4°. The mobile walls in the flux-reversal process at low fields are the invisible plane-parallel walls.

It should be remarked, however, that in the ultrathin tapes there is a large surface-to-volume ratio, and there may be a sufficient orientation of the moments due to

the magnitude of shape anisotropy compared to the crystalline anisotropy to make $\phi' < 4°$. In such a tape the walls created at the intersection of a grain boundary with the surface would be mobile; perhaps in this case the surface may be considered the significant source of mobile walls for flux reversal.

APPENDIX I

To calculate the energy associated with surface poles with the periodic configuration shown in Fig. 2, Eq. (2) is used; the coefficient C_{00} is zero since the configuration represents a demagnetized state. The Fourier coefficients are given by

$$C_{mn}=\frac{2\omega^*}{4\pi^2}\Big\{\int_0^{\beta\pi}\int_0^{\pi}+\int_{(2-\beta)\pi}^{2\pi}\int_0^{\pi}+\int_{(1-\beta)\pi}^{(1+\beta)\pi}\int_{\pi}^{2\pi}+\int_{\beta\pi}^{L_1}\int_{\xi-\beta\pi}^{\pi+\xi-\beta\pi}+\int_{L_1}^{L_2}\int_{A_1}^{\pi+A_1}+\int_{L_2}^{\pi(1-\beta)}\int_{\xi+\beta\pi}^{\pi+\xi+\beta\pi}$$
$$+\int_{\pi(1+\beta)}^{L_3}\int_{A_2}^{\pi+A_2}+\int_{L_3}^{L_4}\int_{A_3}^{\pi+A_3}+\int_{L_4}^{(2-\beta)\pi}\int_{A_4}^{\pi+A_4}\Big\}e^{-i(m\xi+n\eta)}d\eta d\xi,$$

where

$$L_1=\tfrac{1}{2}\pi[1-2\alpha\beta/(1-\alpha)],\quad A_1=(1/\alpha)[\xi-\tfrac{1}{2}\pi(1-\alpha)],$$
$$L_2=\tfrac{1}{2}\pi[1+2\alpha\beta/(1-\alpha)],\quad A_2=-\xi+(2+\beta)\pi,$$
$$L_3=\tfrac{1}{2}\pi[3-2\alpha\beta/(1-\alpha)],\quad A_3=-(1/\alpha)[\xi-\tfrac{1}{2}\pi(3+\alpha)],$$
$$L_4=\tfrac{1}{2}\pi[3+2\alpha\beta/(1-\alpha)],\quad A_4=-\xi+(2+\beta)\pi.$$

It follows that for even n, $C_{mn}=0$ while for odd n,

$$C_{0n}=-\frac{4\omega^*}{\pi^2n^2}\Big\{1+(-1)^{(n+1)/2}(1-\alpha)\sin\Big(\frac{n\beta\pi}{1-\alpha}\Big)\Big\},$$

$$C_{nn}=C_{-nn}=-\frac{4i\omega^*}{\pi^2n^2}\Big\{\frac{3-\alpha}{4(1-\alpha)}\sin(n\beta\pi)+\frac{1}{4}\Big(\frac{1-\alpha}{1+\alpha}\Big)\sin\Big[n\beta\pi\Big(\frac{1+\alpha}{1-\alpha}\Big)\Big]+\frac{n\pi}{2}\Big(\frac{1}{2}-\frac{\beta}{1-\alpha}\Big)\cos(n\beta\pi)\Big\},$$

$$C_{n/\alpha,\,n}=C_{-n/\alpha,\,n}=\frac{2i\alpha\omega^*}{\pi^2n^2}\begin{cases}\Big\{\dfrac{2\alpha^2}{1-\alpha^2}\sin\Big(\dfrac{n\beta\pi}{\alpha}\Big)+\Big[\dfrac{1}{2}\Big(\dfrac{1-\alpha}{1+\alpha}\Big)\sin\Big(\dfrac{2n\beta\pi}{1-\alpha}\Big)+\dfrac{n\beta\pi}{1-\alpha}\Big]\cos\Big[\dfrac{n\pi}{\alpha}\Big(\dfrac{1+\alpha}{2}\Big)\Big]\Big\} & \text{for } n/a \text{ odd integer}\\ \Big\{\dfrac{2\alpha}{1-\alpha^2}\cos\Big(\dfrac{n\beta\pi}{\alpha}\Big)+\Big[\dfrac{1}{2}\Big(\dfrac{1-\alpha}{1+\alpha}\Big)\sin\Big(\dfrac{2n\beta\pi}{1-\alpha}\Big)-\dfrac{n\beta\pi}{1-\alpha}\Big]\cos\Big[\dfrac{n\pi}{\alpha}\Big(\dfrac{1+\alpha}{2}\Big)-\dfrac{\pi}{2}\Big]\Big\} & \text{for } n/\alpha \text{ even integer,}\end{cases}$$

$$C_{mn}=\frac{4i\omega^*}{\pi^2}\Big\{\tfrac{1}{2}(1-\alpha)e^{-i(m+n)\pi/2}\Big[\frac{\sin\Big[\dfrac{(\alpha m+n)\beta\pi}{1-\alpha}\Big]}{(\alpha m+n)(m+n)}-(-1)^m\frac{\sin\Big[\dfrac{(\alpha m-n)\beta\pi}{1-\alpha}\Big]}{(\alpha m-n)(m-n)}\Big]+\begin{cases}\dfrac{n\sin(m\beta\pi)}{m(m^2-n^2)} & \text{if } m \text{ odd}\\ \dfrac{-i\cos(m\beta\pi)}{(m^2-n^2)} & \text{if } m \text{ even}\end{cases}\Big\}.$$

If $L_x=L_y$, then $P_{mn}=(\pi/D)(m^2+n^2)^{\frac{1}{2}}$, and Eq. (2) gives

$$f(\alpha,\beta)=\frac{\sigma_m}{\omega^{*2}D}=\frac{64}{\pi^4}\Big\{\sum_{\substack{1\\ n\text{ odd}}}^{\infty}\Big\{\frac{1}{2n^5}\Big[1+(-1)^{(n+1)/2}(1-\alpha)\sin\Big(\frac{n\beta\pi}{1-\alpha}\Big)\Big]^2$$
$$+\frac{1}{\sqrt{2}n^5}\Big[\frac{3-\alpha}{4(1-\alpha)}\sin(n\beta\pi)+\frac{1}{4}\Big(\frac{1-\alpha}{1+\alpha}\Big)\sin\Big[n\beta\pi\Big(\frac{1+\alpha}{1-\alpha}\Big)\Big]+\frac{n\pi}{2}\Big(\frac{1}{2}-\frac{\beta}{1-\alpha}\Big)\cos(n\beta\pi)\Big]^2\Big\}$$
$$+\sum_{\substack{1\\ n\text{ odd}\\ n/\alpha=\text{odd int.}}}^{\infty}\frac{\alpha^3}{4(1+\alpha^2)^{\frac{1}{2}}}\frac{1}{n^5}\Big\{\frac{2\alpha^2}{1-\alpha^2}\sin\Big(\frac{n\beta\pi}{\alpha}\Big)+\Big[\frac{1}{2}\Big(\frac{1-\alpha}{1+\alpha}\Big)\sin\Big(\frac{2n\beta\pi}{1-\alpha}\Big)+\frac{n\beta\pi}{1-\alpha}\Big]\cos\Big[\frac{n\pi}{\alpha}\Big(\frac{1+\alpha}{2}\Big)\Big]\Big\}^2$$

(Equation continued on next page.)

$$+\sum_{\substack{1\\ n\text{ odd}\\ n/\alpha=\text{even int.}}}^{\infty}\frac{\alpha^3}{4(1+\alpha^2)^{\frac{1}{2}}}\frac{1}{n^5}\left\{\frac{2\alpha}{1-\alpha^2}\cos\left(\frac{n\beta\pi}{\alpha}\right)+\left[\frac{1}{2}\left(\frac{1-\alpha}{1+\alpha}\right)\sin\left(\frac{2n\beta\pi}{1-\alpha}\right)-\frac{n\beta\pi}{1-\alpha}\right]\cos\left[\frac{n\pi}{\alpha}\left(\frac{1+\alpha}{2}\right)-\frac{\pi}{2}\right]\right\}^2$$

$$+\sum_{\substack{1\\ n,m\\ m\neq n,\ n/\alpha}}^{\infty}\sum_{\text{odd}}^{\infty}\left\{\frac{n}{m}(\alpha^2m^2-n^2)\sin(m\beta\pi)+(-1)^{(m+n)/2}\left[(1-\alpha)(\alpha m^2+n^2)\sin\left(\frac{\alpha m\beta\pi}{1-\alpha}\right)\cos\left(\frac{n\beta\pi}{1-\alpha}\right)\right.\right.$$

$$\left.\left.-mn(1-\alpha^2)\cos\left(\frac{\alpha m\beta\pi}{1-\alpha}\right)\sin\left(\frac{n\beta\pi}{1-\alpha}\right)\right]\right\}^2\Big/(\alpha^2m^2-n^2)^2(m^2-n^2)^2(m^2+n^2)^{\frac{1}{2}}$$

$$+\sum_{\substack{1\\ n\text{ odd},\ m\\ m\neq n/\alpha}}^{\infty}\sum_{\text{even}}^{\infty}\left\{(\alpha^2m^2-n^2)\cos(m\beta\pi)+(-1)^{(m+n-1)/2}\left[(1-\alpha)(\alpha m^2+n^2)\sin\left(\frac{n\beta\pi}{1-\alpha}\right)\cos\left(\frac{\alpha m\beta\pi}{1-\alpha}\right)\right.\right.$$

$$\left.\left.-mn(1-\alpha^2)\cos\left(\frac{n\beta\pi}{1-\alpha}\right)\sin\left(\frac{\alpha m\beta\pi}{1-\alpha}\right)\right]\right\}^2\Big/(\alpha^2m^2-n^2)^2(m^2-n^2)^2(m^2+n^2)^{\frac{1}{2}}\Bigg\}. \quad \text{(I.1)}$$

It is interesting to first examine the two special cases $f(0,\beta)$ and $f(\alpha,\frac{1}{2}(1-\alpha))$, which follow directly from Eq. (I.1) as

$$f(0,\beta)=\frac{64}{\pi^4}\Bigg\{\sum_{\substack{1\\ n\text{ odd}}}^{\infty}\frac{[1+(-1)^{(n+1)/2}\sin(n\beta\pi)]^2}{2n^5}+\frac{[\sin(n\beta\pi)+(\frac{1}{2}-\beta)(n\pi/2)\cos(n\beta\pi)]^2}{\sqrt{2}n^5}$$

$$+\sum_{\substack{1\\ n,m\\ m\neq n}}^{\infty}\sum_{\text{odd}}^{\infty}\frac{[(n/m)\sin(m\beta\pi)+(-1)^{(m+n)/2}(m/n)\sin(n\beta\pi)]^2}{(m^2-n^2)^2(m^2+n^2)^{\frac{1}{2}}}$$

$$+\sum_{\substack{1\\ n\text{ odd}\\ m}}^{\infty}\sum_{\text{even}}^{\infty}\frac{[(-1)^{(m+n+1)/2}\sin(n\beta\pi)+\cos(m\beta\pi)]^2}{(m^2-n^2)^2(m^2+n^2)^{\frac{1}{2}}}\Bigg\}, \quad \text{(I.2)}$$

$$f(\alpha,\tfrac{1}{2}(1-\alpha))=\frac{64}{\pi^4}\Bigg\{\sum_{\substack{1\\ n\text{ odd}}}^{\infty}\frac{\alpha^2}{2n^5}+\sum_{\substack{1\\ n,m\\ m\neq n/\alpha}}^{\infty}\sum_{\text{odd}}^{\infty}\frac{[1+\cos(\alpha m\pi)]n^2}{2m^2(\alpha^2m^2-n^2)^2(m^2+n^2)^{\frac{1}{2}}}+\sum_{\substack{1\\ n\text{ odd}\\ m\text{ even}\\ m\neq n/\alpha}}^{\infty}\sum_{2}^{\infty}\frac{[1+\cos(\alpha m\pi)]\alpha^2}{2(\alpha^2m^2-n)^2(m^2+n^2)^{\frac{1}{2}}}$$

$$+\sum_{\substack{1\\ n/\alpha=\text{int.}\\ n\text{ odd}}}^{\infty}\frac{\pi^2\alpha^3}{16(1+\alpha^2)^{\frac{1}{2}}}\frac{1}{n^3}\Bigg\}. \quad \text{(I.3)}$$

The curves for $f(\alpha,\beta)$ of Figs. 4 and 5 are calculated from Eqs. (I.3) and (I.2), respectively. The curves for $\Delta\sigma/\omega^{*2}D'$ follow from the relation:

$$\Delta\sigma/\omega^{*2}D'=3.4-2f(\alpha,\beta)(D/D')-1.7s(\alpha,\beta)(D'/D), \quad \text{(I.4)}$$

where $s(\alpha,\beta)$ is the length of domain-wall intercept with the surface in the area D^2. The curves of Fig. 6 are calculated from Eqs. (I.1) and (I.4).

APPENDIX II

If the restriction $L_x=L_y$ is removed and a variable parameter $\gamma=L_y/L_x$ is introduced, then $D=\gamma\pi L_x=\pi L_y$ and $P_{mn}=\pi(\gamma^2m^2+n^2)^{\frac{1}{2}}/D$. In the case $\beta=(1-\alpha)/2$, Eq. (I.3) is modified to

$$f(\alpha,\gamma)=\frac{64}{\pi^4}\Bigg\{\sum_{\substack{1\\ \text{odd } n}}^{\infty}\frac{\alpha^2}{2n^5}+\sum_{\substack{1\\ \text{odd } n\\ m\neq n/\alpha}}^{\infty}\sum_{n,m}^{\infty}\frac{[1+\cos(\alpha m\pi)]n^2}{2m^2(\alpha^2m^2-n^2)^2(\gamma^2m^2+n^2)^{\frac{1}{2}}}$$

$$+\sum_{\substack{1\\ \text{odd } n\\ \text{even } m\neq n/\alpha}}^{\infty}\sum_{2}^{\infty}\frac{[1+\cos(\alpha m\pi)]\alpha^2}{2(\alpha^2m^2-n^2)^2(\gamma^2m^2+n^2)^{\frac{1}{2}}}+\sum_{\substack{1\\ \text{odd } n\\ n/\alpha=\text{int.}}}^{\infty}\frac{\pi^2\alpha^3}{16(\gamma^2+\alpha^2)^{\frac{1}{2}}}\cdot\frac{1}{n^3}\Bigg\}. \quad \text{(II.1)}$$

If the walls are everywhere perpendicular to the surface, the area of wall per unit top-surface area is $Ls(\alpha,\gamma)/D^2$, where

$$s(\alpha,\gamma)=[1-\alpha+(\alpha^2+\gamma^2)^{\frac{1}{2}}]D/\gamma \tag{II.2}$$

and the change in energy per unit top-surface area on going from a parallel-wall to a trapezoidal configuration is $\Delta\sigma$, where

$$\Delta\sigma/\omega^{*2}D'=3.4-2f(\alpha,\gamma)D/D'-1.7[1-\alpha+(\alpha^2+\gamma^2)^{\frac{1}{2}}]D'/D.$$

Since the optimum value of D/D' is $\{1.7[1-\alpha+(\alpha^2+\gamma^2)^{\frac{1}{2}}]/2f(\alpha,\gamma)\}^{\frac{1}{2}}$, this change in energy is

$$\Delta\sigma(\alpha,\gamma)/\omega^{*2}D'=3.4-2\{3.4[1-\alpha+(\alpha^2+\gamma^2)^{\frac{1}{2}}]f(\alpha,\gamma)\}^{\frac{1}{2}}. \tag{II.3}$$

In Fig. 7 are plotted $f(\frac{1}{2},\gamma)$ and $\Delta\sigma(\frac{1}{2},\gamma)/\omega^{*2}D'$ as calculated from Eqs. (II.1) and (II.3).

If the domain walls are not perpendicular to the surface, but taper toward a plane wall within the interior of the material as shown in Fig. 8, then instead of $Ls(\alpha,\gamma)$ it is necessary to calculate

$$2\int_0^{L/2} s(z)dz=\frac{D}{\gamma}\int_0^{D/2\lambda}(1-\alpha+[\alpha^2+\gamma^2(1-2\lambda z/D)^2]^{\frac{1}{2}}dz+L/2-D/(2\lambda)$$

$$=\frac{D}{\gamma}\left(\frac{D}{2\lambda}\right)\left\{\left(\frac{\lambda L}{D}-\alpha\right)+\frac{1}{2}\left[(\alpha^2+\gamma^2)^{\frac{1}{2}}+\frac{\alpha^2}{\gamma}\ln\left(\frac{\gamma+(\alpha^2+\gamma^2)^{\frac{1}{2}}}{\alpha}\right)\right]\right\},$$

where $D/2\lambda$ is the depth beneath the surface at which the wall becomes planar if a uniform taper to that depth is assumed. In the special case $D/2\lambda=L/2$,

$$2\int_0^{L/2} s(z)dz=\frac{D}{\gamma}Lp(\alpha,\gamma),$$

where

$$p(\alpha,\gamma)=1-\alpha+\frac{1}{2}\left[(\alpha^2+\gamma^2)^{\frac{1}{2}}+\frac{\alpha^2}{\gamma}\ln\left(\frac{\gamma+(\alpha^2+\gamma^2)^{\frac{1}{2}}}{\alpha}\right)\right].$$

In this case Eq. (II.3) must be modified to

$$\Delta\sigma(\alpha,\gamma)/\omega^{*2}D'=3.4-2\{3.4p(\alpha,\gamma)f(\alpha,\gamma)\}^{\frac{1}{2}}-\sigma_d/\omega^{*2}D',$$

where σ_d is the energy per unit top-surface area due to the magnetic poles at the domain walls which result from the angle the tapered walls make with the magnetization within the domains. In order to have $\Delta\sigma>0$, it is necessary to have

$$0<\sigma_d/\omega^{*2}D'<3.4-2\{3.4p(\alpha,\gamma)f(\alpha,\gamma)\}^{\frac{1}{2}}. \tag{II.4}$$

In Fig. 7 there is also plotted

$$(\Delta\sigma+\sigma_d)/\omega^{*2}D'=3.4-2\{3.4p(\tfrac{1}{2},\gamma)f(\tfrac{1}{2},\gamma)\}^{\frac{1}{2}}.$$

as a function of γ.